CrossMark

RESEARCH PAPER

Bistability in the hydrodynamic resistance of a drop trapped at a microcavity junction

Swastika S. Bithi[1] · **Mehdi Nekouei**[1] · **Siva A. Vanapalli**[1]

Abstract We investigate the flow resistance of a droplet trapped at a constriction in a microcavity located at a microchannel bifurcation as a function of system parameters including capillary number, drop confinement, and viscosity ratio. Using a combination of experiments and volume-of-fluid numerical simulations, we measure the hydrodynamic resistance of the trapped drop and connect it to drop deformation in the microcavity. For drop sizes smaller than the microcavity, we observe a bistable behavior in terms of the resistance of the trapped drop as a function of capillary number. For these underfilled drops, we find that the resistance is low at small capillary number ($Ca < 10^{-3}$) and jumps to high resistance at a threshold capillary number. For drops equal to the microcavity size, we observe that the bistability vanishes and the drop resistance is of similar magnitude as that of underfilled drops at large capillary number. To explain these findings, we use confocal microscopy and simulations to obtain three-dimensional views of the drop deformation and continuous phase fluid in the microcavity. We observe that the low resistance is due to negligible drop deformation and unobstructed flow of continuous phase through the constriction. The high resistance is due to the drop interface protruding into the constriction restricting the flow of continuous phase through the gutters. Taken together, our results indicate that a trapped drop at a bifurcation can act as a nonlinear resistor and could be potentially used as a soft switch to control droplet trajectories in microfluidic devices.

Swastika S. Bithi and Mehdi Nekouei have contributed equally.

✉ Siva A. Vanapalli
siva.vanapalli@ttu.edu

1 Department of Chemical Engineering, Texas Tech University, Lubbock, TX 79409, USA

1 Introduction

Trapping or physical immobilization of droplets in confined microfluidic channels is widely used in the field of drop-based microfluidics where droplets are employed as microreactors for biological and chemical analysis (Pompano et al. 2011; Seemann et al. 2011). For example, arrays of trapped microfluidic droplets have been used for DNA analysis (Zhang and Xing 2010), nucleation studies (Edd et al. 2009), cell-based assays, (Bithi and Vanapalli 2017; Jeong et al. 2015; Shemesh et al. 2014) and protein crystallization investigations (Du et al. 2009; Lau et al. 2007). In these applications, trapped droplets are essential as they allow simultaneous monitoring of reactions in individual droplets or storage of samples for a desired duration before further processing.

A variety of geometric configurations have been used to trap microfluidic droplets ranging from microcavities (Bithi and Vanapalli 2010; Bithi et al. 2014; Boukellal et al. 2009; Shi et al. 2008; Sun et al. 2011) to surface energy wells (Dangla et al. 2011) to rails and anchors (Fradet et al. 2011). Here, we use a microcavity that is connected to a bypass channel as shown in Fig. 1a to trap a droplet and characterize its hydrodynamic resistance as a function of system parameters. This geometry has been shown to be a flexible configuration for trapping droplets, creating droplets of controlled composition by momentarily coalescing incoming droplets with the drops in the cavities, and for washing the contents of a stored drop while retaining the suspended particles (Bithi and Vanapalli 2015; Bithi et al. 2014).
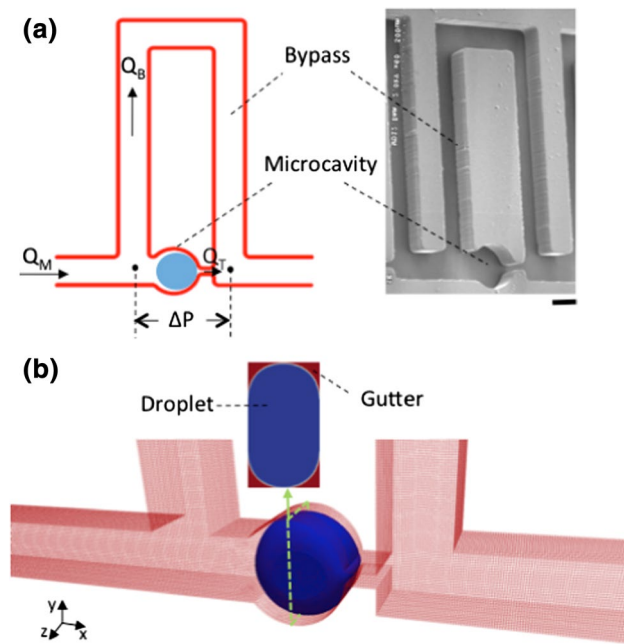
Despite the practical significance of trapped microfluidic droplets for lab-on-chip applications, the hydrodynamic resistance and flow response of a trapped droplet in a cavity has not been fundamentally addressed. When a drop is trapped at a constricted microchannel the

Fig. 1 Channel geometry used to trap a drop and measure flow resistance. **a** (Left) schematic of the bypass geometry used to trap the droplet. The variables used to determine the hydrodynamic resistance of the trapped drop are highlighted. (Right) Scanning electron micrograph of the bypass geometry with trap and constriction. Scale bar is 200 μm. **b** A section of the bypass geometry rendered from the 3-D VOF simulation is shown with a droplet trapped in the microcavity. Inset shows the cross-sectional (y–z) view of the trapped drop (blue) and the continuous phase that flows through the gutters (red) (color figure online)

continuous phase can flow through the lubricating thin films and gutters (Fig. 1b). The drop can be deformed based on the competition between fluid pressure, shear, and interfacial stresses, before it squeezes through the constriction (Huerre et al. 2015; Ling et al. 2016; Zhu and Gallaire 2016). In particular, due to the blockage imposed by the trapped drop, the pressure drop is expected to increase. However, to our knowledge, the pressure drop versus flow rate relation that results from obstruction of fluid flow and the concomitant deformation of the trapped drop has not been reported. Likewise, it is unknown how the drop viscosity and the degree of confinement in the cavity influence the flow resistance. This basic knowledge is crucial for lab-on-chip applications where flow conditions need to be optimized for trapping drops and assay fluids may have different viscosity. In addition, the flow resistance determines the leaky flow rate in the gutters, which can affect the ability of an incoming drop to coalesce with the trapped drop—a control feature that is of significant importance for metering, dilution, and lock-shift operations in drop-based microfluidics (Bithi et al. 2014; Korczyk et al. 2013; Sun et al. 2011; Zagnoni and Cooper 2010).

In this study, using a combination of experiments and volume-of-fluid (VOF) numerical simulations, we investigate the hydrodynamic resistance due to a drop trapped at a microcavity junction. By knowing the flow rate Q_T and the pressure drop ΔP across the droplet (see Fig. 1a), the hydrodynamic resistance R_{td} due to the trapped drop can be determined as $\Delta P/Q_T$. In general, the hydrodynamic resistance of a droplet trapped in a microcavity could be affected by several parameters including capillary number, viscosity ratio, droplet confinement, surfactant concentration, and wettability of the channel walls. In this work, we focus on drops with no added surfactant and investigate the effect of the following system parameters: (1) capillary number, defined as the ratio of viscous to interfacial stresses, i.e. $Ca = \mu_o U/\gamma$, where μ_o is the viscosity of the continuous phase and U is the fluid velocity scale (defined in Sect. 3) and γ is the interfacial tension, (2) viscosity ratio, defined as the ratio of drop fluid viscosity to the continuous phase viscosity, i.e. $= \mu_r/\mu_o$, (3) drop confinement, defined as the ratio of drop diameter to the trap diameter, i.e. $\alpha = D/d$, and (4) the channel aspect ratio, defined as the ratio of main channel height to width, i.e. $H = h/w$. The range of these parameters covered in the experiments are $Ca = 10^{-4}$–10^{-2}; $\lambda = 0.03, 1, 17$; $\alpha = 0.6, 0.8$, and 1; $H = 1$. A similar range was covered in numerical simulations with an added aspect ratio of $H = 0.25$.

The paper is organized as follows. In Sect. 2, we describe the materials and methods that are used in the study. In Sect. 3.1, we present our experimental and VOF numerical approach for determining the flow resistance of a trapped drop. In Sect. 3.2, we discuss the variation of pressure drop with flow rate in the presence of a trapped droplet including the influence of drop viscosity ratio and channel aspect ratio. In Sects. 3.3 and 3.4, we characterize the drop deformation and connect it to the flow resistance behavior that includes a nonlinear transition.

2 Materials and methods

2.1 Device fabrication

We fabricated polydimethyl siloxane (PDMS) devices using soft lithography (Duffy et al. 1998). Our device has two basic units: (1) a droplet generator based on T-junction geometry and (2) a drop storage zone that consists of a microfluidic parking network (MPN) (Bithi et al. 2014). The MPN consists of serially linked fluidic parking loops, where each parking loop contains a main entry channel, bypass channel, and a lower branch containing a fluidic trap (Fig. 1a). Experiments were conducted with a single device geometry in which the width and height of the main channel is 200 μm, yielding an aspect ratio $H = 1$. The bypass channel width and length are 200 and

4000 µm, respectively. The trap size, the width, and length of the constriction after the hydrodynamic trap are 320, 40, and 100 µm, respectively. All features in the device have a uniform height of 200 µm. The ratio of resistance of the bypass to the trap channel is $R_B/R_T = 1.5$. The scanning electron micrograph (Fig. 1a) was obtained from an unbounded PDMS slab of a parking loop using Hitachi S-4300 scanning electron microscope.

2.2 Materials

The dispersed phase is either water or aqueous solutions of glycerol. The continuous phase used in the experiments was a solution of 0.5 wt% polystyrene beads (3 µm diameter) in embryonic mineral oil (Sigma Aldrich, Part M5904, $\mu_o = 30$ mPa s) with no added surfactant, $\gamma = 50$ mN/m (measured using Kruss K100 tensiometer, Kruss, NC). During confocal fluorescence imaging, the continuous phase was visualized using 0.3 wt% of Nile red in mineral oil.

2.3 Drop storage procedure

Trains of small confined drops without surfactant were injected into the MPN by controlling the aqueous and oil flow rates Q_w and Q_o at an upstream T-junction, using syringe pumps (PHD2000, Harvard Apparatus). We used three different aqueous flow rates ($Q_w = 50, 80, 100$ µL/h) with a fixed oil flow rate ($Q_o = 100$ µL/h) to get different sizes of drops. For $\alpha = 1$, we utilize hydrodynamic self-rectification (Bithi et al. 2014) where the generated drops from the T-junction coalesce with trapped drops and rectify the parked drop volume to yield a volume equal to the trap volume. We trapped several drops in the whole MPN; however, we focused on the first drop for our investigation.

Experiments were performed on inverted microscope (Olympus IX70, IX71). Images were taken under bright field mode using high-speed camera (Phantom V310) at 700–3200 fps at the mid-plane of the device. The diameters of at least ten trapped drops were measured using Image J software. The standard deviation in α was less than 3%.

2.4 Particle tracking velocimetry

We pumped a solution of 0.5 wt% polystyrene beads (3 µm diameter) in mineral oil into the MPN (Fig. 2a). Typically 10–15 tracer particles were tracked at the intersection of the horizontal and vertical mid-planes (along the height and the width of the channel) in both the main channel and the bypass of the loop. The calculated velocity of these tracer particles at the midplane corresponds to the maximum fluid velocity (V_{max}) in the respective channel. The average fluid velocity is then given by,

$$V_{avg} = \beta V_{max} \tag{1}$$
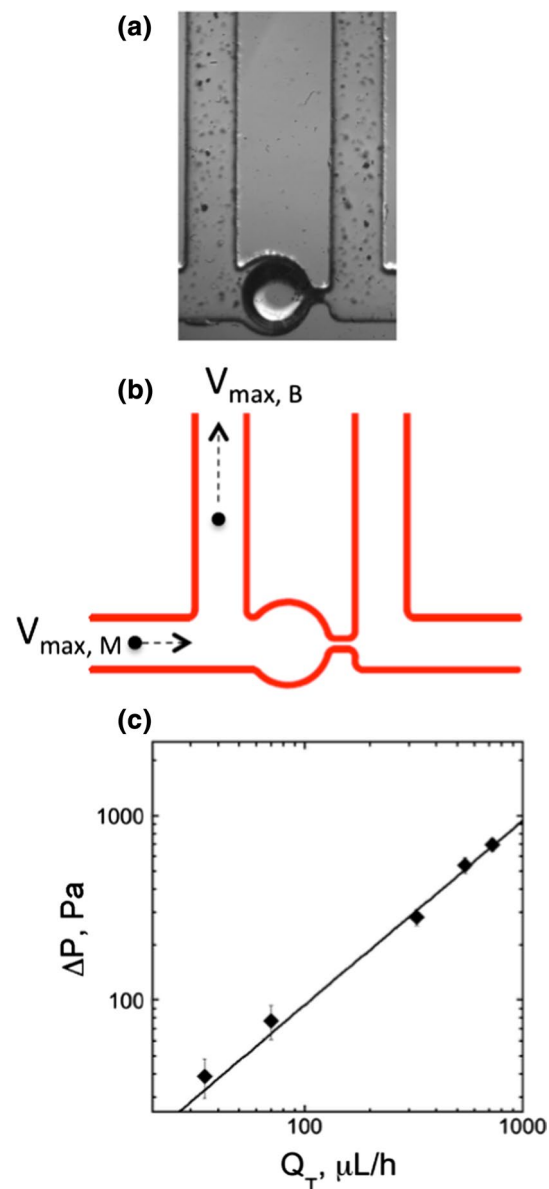
Fig. 2 Principle of measuring pressure drop due to a trapped droplet. **a** Image showing tracer particles seeded in the fluid to measure the flow rate in the bypass. **b** Schematic showing the principle of single-point particle tracking velocimetry to quantify the ratio of velocities in inlet and bypass channels. **c** The pressure drop ΔP between the junctions of the two parallel paths in the parking loop in the absence of a trapped drop as a function of flow rate through the trap (Q_T). The symbols denote experimental data, and the line indicates analytical result (see main text for details)

where β is the proportionality constant that depends on the height and width of the channel. The proportionality constant β is the same for the main channel and the bypass as the height and width of these channels are identical. We find the standard deviation of the velocity measurements is at most 20%. This standard deviation is mostly due to syringe

pump-induced flow fluctuations that introduce variability in particle positions.

2.5 Visualization of continuous phase around the trapped drop

To visualize the continuous phase around the trapped drop, fluorescent tracer (Nile red) was added to the continuous phase and the water drop was captured in the trap. Flow rates of the continuous phase were varied until the drop squeezed through the constriction. We used 3i Marianas spinning disk confocal system (Intelligent Imaging Innovations, Inc., CO) equipped with Evolve EMCCD camera to image the layer of continuous phase fluid surrounding the trapped drop. Imaging was done with a 20× objective providing a pixel resolution of 1 μm per pixel. The z-stack was obtained by scanning depthwise in steps of 1 μm. Three-dimensional rendering of the image stack was done using Slidebook 6 software.

2.6 VOF simulation

VOF is implemented in *interFoam* solver in OpenFOAM (OpenCFD 2009). We have reported the details of the implementation of VOF and benchmarked the solver for droplet production in microfluidics in our recent paper (Nekouei and Vanapalli 2017). The use of this solver for droplet and bubble flows in microchannels has also been reported in several papers (Hoang et al. 2013a, b; Nieves-Remacha et al. 2015).

In our simulation, we have used the experimental geometry that is shown in Fig. 1b. We have used ANSYS gambit to mesh this geometry. For the boundary conditions, constant velocity and constant pressure are imposed at the inlet and outlet of the system, respectively. At walls of the channels, no slip boundary condition is applied. Since the dispersed phase is not wetting the walls, the static angle is set to be constant at 180° at the walls. In our simulations, the droplet is located at the center of the trap initially, and then we impose the flow rate at the inlet. In these simulations, we have gradually increased the inlet flow rate and computed the pressure drop across the trapped drop.

3 Results

3.1 Experimental determination of flow resistance of a trapped drop

We employ a unique experimental strategy coupled with particle tracking velocimetry (PTV) that allows not only easy trapping of drops but also enables determination of flow resistance without the use of microfluidic manometers to measure pressure drop (Abkarian et al. 2006; Vanapalli et al. 2007, 2009) or characterization of the full velocity field in

microchannels to quantify flow rates. As shown in Fig. 2a, we employ a microfluidic parking loop that contains a microcavity to trap a drop and a bypass channel. The microcavity contains a constriction that prevents the drop from squeezing. Previously, it has been shown that an MPN could be used to trap an array of droplets in different ways—using either small drops or long plugs, with or without surfactant-coverage (Bithi and Vanapalli 2010, 2015; Bithi et al. 2014; Boukellal et al. 2009; Shi et al. 2008; Sun et al. 2011). Here, we used an upstream T-junction and generated drops that are not coated with surfactants and operated in a special flow regime called *hydrodynamic self-rectification* to trap droplets in MPNs (see Bithi et al. 2014 for more details). During hydrodynamic self-rectification, the generated drops from the T-junction coalesce with trapped drops, rectifying any non-uniformity in the parked drop volume. Therefore, this method enables easy trapping of droplets over a wide range of flow conditions and injected drop sizes, making the trapping process essentially uncoupled to drop production and largely insensitive to network geometry (Bithi et al. 2014). We also used the rectification method to trap droplets of different viscosities.

We take advantage of the bypass channels in MPNs to quantify the pressure drop versus flow rate relation for a trapped drop. We do this by (1) pursuing single-point velocity measurements of flow in the bypass channel to determine the continuous phase flow rate in the bypass and the main channel, and (2) applying resistive circuit analysis to determine the pressure drop across the parking loop. We discuss these two aspects of our measurement technique below.

We seed the continuous phase with tracer particles as shown in Fig. 2a. The velocity of a given particle (usually at the centerline and in the vertical midplane) in both the main inlet and the bypass channels—$V_{max,M}$ and $V_{max,B}$, respectively—is measured (see Fig. 2b). Knowing the main channel flow rate Q_M imposed by the syringe pump, the flow rate Q_B in the bypass can be calculated as

$$Q_B = \frac{V_{max,B}}{V_{max,M}} Q_M \tag{2}$$

The fluid flow rate through the trap is then estimated from mass conservation as

$$Q_T = Q_M - Q_B \tag{3}$$

Finally, the pressure drop across the trap is given by

$$\Delta P = Q_B R_B \tag{4}$$

since the bypass is connected in parallel with the trap channel. We calculate analytically the hydraulic resistance of the bypass, R_B, from known channel geometry (Bruus 2008). Thus, Eqs. (2)–(4) allow us to determine the ΔP versus Q_T relation for a trapped droplet.

To validate this method, we measured the pressure drop between the junctions of the parking loop in the *absence* of a trapped drop and compared the experimental data with theory (Fig. 2c). We varied the main channel flow rate and measured the flow rate in the bypass by applying the single-point particle tracking technique described above. As expected, the measured ΔP varied linearly with the flow rate in the trap channel (see symbols in Fig. 2c). We compared this data with the predicted pressure drop, $\Delta P = R_T Q_T$. Here, R_T is the hydrodynamic resistance for the bottom branch containing the trap, which was calculated by assuming the trap chamber and constriction are in series and using the analytical equations for hydraulic resistance of rectangular ducts (Bruus 2008). As shown in Fig. 2c, we find excellent agreement between measured and predicted pressure drop data, with the error being 10 and 20% at high and low flow rates (< 400 µL/h input flow rates), respectively. The higher error at low flow rates is probably due to pump-induced flow fluctuations (Korczyk et al. 2011; Li et al. 2014).

### 3.2 Pressure drop variation with flow rate for a trapped drop

In this section, we discuss results from our experiments and simulations on how the pressure drop across the trapped droplet varies as a function of the flow rate in the trap channel, including the influence of drop confinement, viscosity ratio, and channel aspect ratio. In both the experiments and simulations, the main channel flow rate was varied—as a result, the flow rates in the trap and bypass channels were allowed to adjust depending on the resistance of the trapped drop. In addition, for all the conditions tested, we recorded the pressure drop data up to the point of squeezing of the drops through the constriction.

Figure 3a shows the dependence of the experimentally measured pressure drop across the trapped droplet as a function of flow rate of the trapped channel, for three different viscosity ratios $\lambda = 0.03$, 1, and 17, three values of drop confinement $\alpha = 0.6$, 0.8, and 1, and channel aspect ratio $H = 1$. For drop sizes smaller than the trap ($\alpha = 0.6, 0.8$), i.e. underfilled drops, we observe that at low flow rates, the pressure drop increases linearly with flow rate which we refer to as *state I*. Beyond a certain flow rate, there is a steep jump in the pressure drop, which we refer to as the transition zone (discussed further in Sect. 3.4). At higher flow rates, we observe another linear increase in pressure drop with flow rate, which we refer to as *state II*. In contrast, this two-state or bistable behavior disappears for drops with $\alpha = 1$, i.e. when the drop fully fills the trap and the pressure drop profile follows that of *state II*.

The bistable behavior is much more evident for the data corresponding to $(\lambda, \alpha) = (0.03, 0.6)$ and $(\lambda, \alpha) = (17, 0.8)$ than the other two tested conditions due to more experimental data points. In addition, we do not observe a strong influence of the drop viscosity on the measured pressure drop. We pursue linear fits to the ΔP versus Q_T data and find that the magnitude of the pressure drop due to the trapped drop in *state I* and *state II* is ≈ 2 and ≈ 16 times higher than the no-drop case, respectively, suggesting stronger occlusion of the constriction by the drop in *state II*. For the $\alpha = 1$ case, $\Delta P \approx 16 Q_T$, the same as *state II*.

To further corroborate the experimental observations, we performed numerical simulations, which allowed us to access lower trap flow rates than experiments. Figure 3b shows the results of our simulations for viscosity ratio $\lambda = 0.03$ and 17 and three different drop sizes $\alpha = 0.6$, 0.8 and 1. For drop sizes smaller than the trap ($\alpha = 0.6, 0.8$), we observe that there are two states of pressure drop behavior

Fig. 3 Pressure drop versus flow rate behavior for trapped drops. **a** Experiment. **b** VOF simulation. Different symbols represent the viscosity ratios of inner phase to outer phase for different drop sizes. The viscosity ratios were obtained by varying the inner phase viscosity while keeping the outer phase fixed. Error bars represent the standard deviation in measurements. The solid lines are the best fits to the data corresponding to the States I and II. The dashed line represents the analytical equation for the no-drop case, also shown in Fig. 2c. The data here corresponds to channel aspect ratio $H = 1$
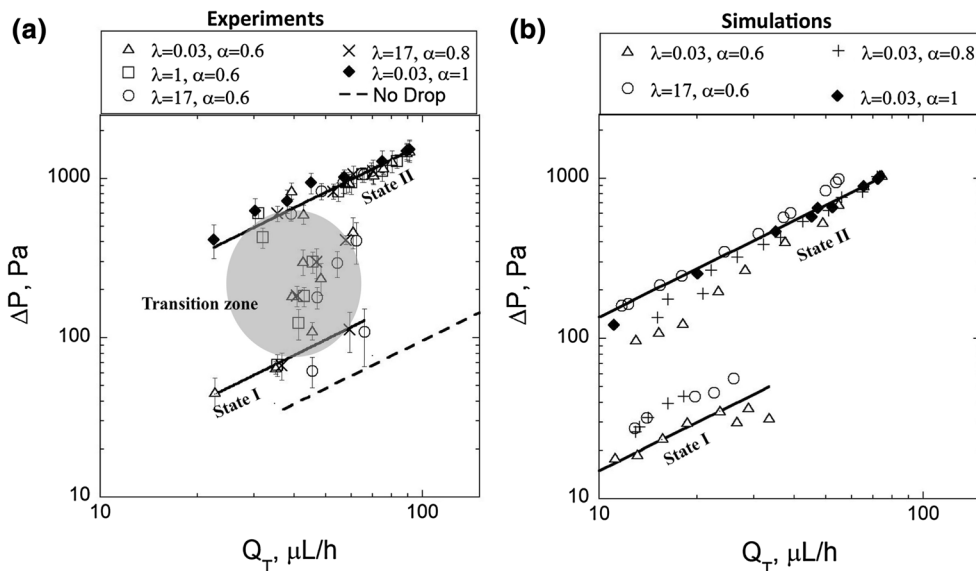
for low and high flow rates, similar to the experimental results. Although in experiments we are unable to discern the influence of drop viscosity, in simulations we find that the drop viscosity has a minor influence, with higher-viscosity drops offering slightly larger resistance. This is plausible, since the interface of the higher-viscosity drops is less mobile than lower-viscosity drops, offering more resistance for the continuous phase to flow through the gutters.

The transition region is observed to be much more dramatic in the simulations compared to the experiments, as evidenced by the abrupt jump from *state I* to *state II* without any data points in between the two states. Interestingly, for $\alpha = 1$, a fully confined drop, the bistable behavior vanishes, and we observe the *state II* pressure drop behavior only—both in experiment (Fig. 3a) and in simulation (Fig. 3b).

We also compared the slopes in simulations and experiments corresponding to the linear behavior in the two states. In simulations, we find the slopes for *state I* and *state II* to be ~ 1.5 and ~ 14, respectively. These slopes are of the same order as experiments, but slightly lower. This discrepancy could arise due to the need for even finer mesh in simulations and/or due to slight differences in the wettability characteristics of the channel walls between experiments and simulations.

Next, we investigated the influence of channel aspect ratio on the bistability and flow resistance of a trapped drop, using VOF simulations. We chose a channel aspect ratio of 0.25 and drop size with $\alpha = 0.6$. We found the pressure drop and the resistance of the trapped drop follow the bistable behavior similar to the system with aspect ratio of 1 (Fig. 4). However, the *state I* is associated with higher pressure drop values, while the pressure drop range for *state II* remains similar. In addition, the transition to bistability occurs at lower flow rates because the reduced gutter size at $H = 0.25$
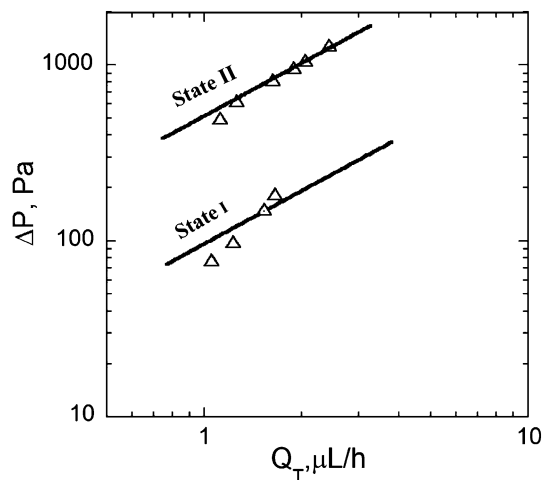
causes the pressure drop to increase and therefore deforms the drop at lower Q_T.

3.3 Connecting flow resistance to drop deformation: origin of bistability

In the previous section, we characterized the pressure drop behavior of the trapped drop using a combination of experiments and simulations. Here, we translate the pressure drop versus flow rate data into hydrodynamic resistance versus capillary number. We also monitor the deformation of the trapped drop and relate the deformed configuration to the observed flow resistance and bistability behavior.

Figures 5 and 6 show the hydrodynamic resistance as a function of capillary number from experiments and simulations, respectively. Here, the resistance of the trapped drop is normalized by the resistance of the empty trap-branch R_T, and the velocity scale in the capillary number definition is taken as the mean velocity corresponding to Q_M. Consistent with the two-state pressure drop behavior, the resistance of the trapped drop also shows bistable behavior with a transition zone (Fig. 5a) for drop sizes smaller than the trap ($\alpha = 0.6, 0.8$). Due to the linear profiles of ΔP versus Q_T, the flow resistance is almost constant in *state I* and *state II* and is largely independent of drop viscosity.

To understand the bistable behavior, we visualized the three-dimensional deformation of the trapped drop ($\alpha = 0.6$) using confocal microscopy, since it is expected that the
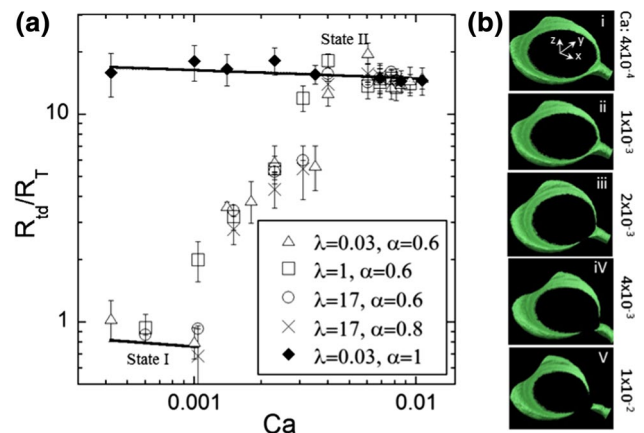
Fig. 5 Connecting flow resistance of a trapped drop to its deformation. **a** Experimental data showing the normalized resistance of the trapped drop as function of the capillary number Ca. Here, the drop resistance is normalized with the hydrodynamic resistance of the trap-branch $R_T = 3.4$ kg/(s mm^4). Data is shown for drops of different viscosity ratio λ and confinement α. The error bar represents the standard deviation in R_{td} measurement. The lines represent the best fits to the data at low and high Ca. **b** Confocal 3-D rendering of image volumes (*i–v*) of a trapped drop with $\alpha = 0.6$, at various capillary numbers. Fluorescent dye has been added to the continuous phase. The data shown here are for $H = 1$

Fig. 4 Simulation results on the effect of channel aspect ratio on the bistability behavior for $H = 0.25$ and $\alpha = 0.6$ and $\lambda = 0.03$
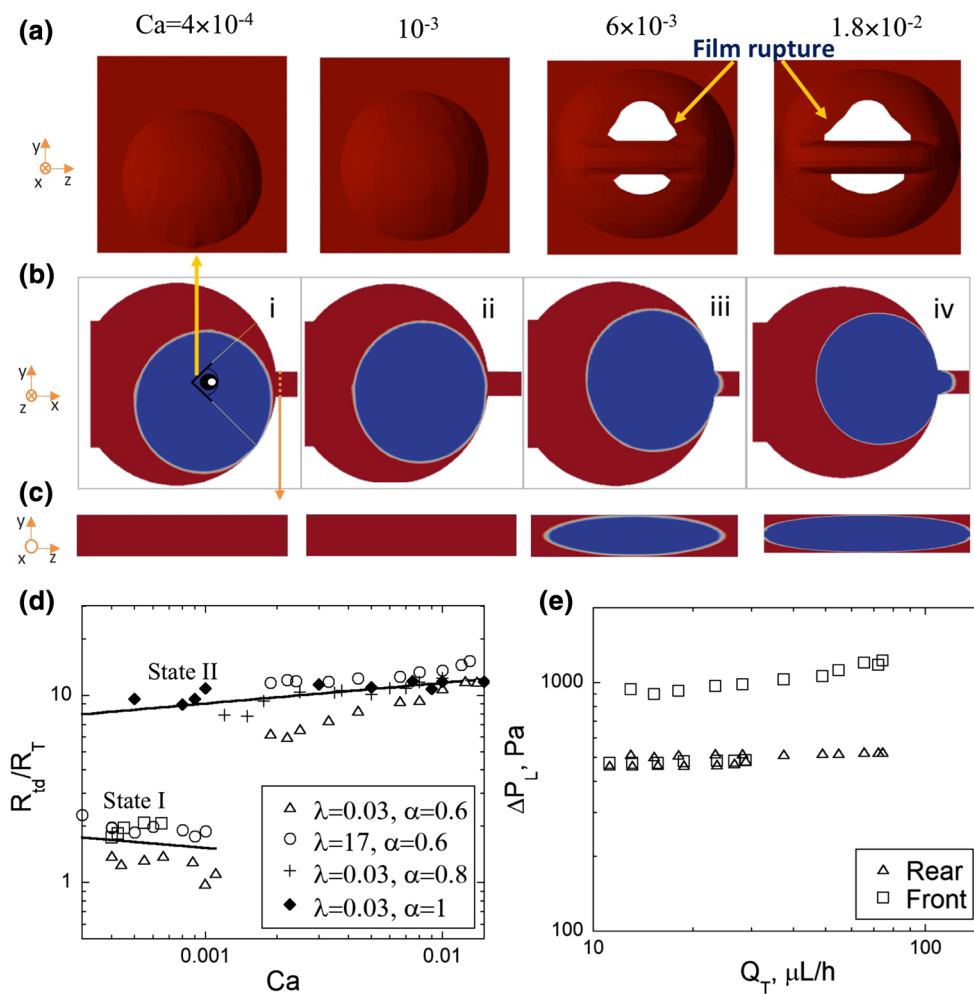
Fig. 6 Hydrodynamic resistance and morphology of the trapped droplet at selected Ca in simulations. **a** End-view images showing the continuous phase around the droplet. The drop phase (in blue) is not shown intentionally. The end-views were obtained by looking [see the direction of eye shown in (**b**)-i] at the continuous phase near the constriction. With increase in Ca, the droplet touches the front wall and the continuous phase film appears to rupture. **b** The midplane view of the droplet. As we increase Ca, the penetration of drop interface into the constriction increases. **c** The cross section images depict the occu-pancy of the constriction by drop fluid at different Ca. By increasing Ca, the gutter area reduces. **d** Normalized resistance as a function of capillary number. The lines represent the best fits to the data at low and high Ca. **e** The Laplace pressure jump (ΔP_L) at the front (i.e. toward constriction) and rear interface of the drop is shown as a function of the flow rate in the trap. ΔP_L was measured in the simulation at the symmetry axis of the main channel, just across the front and rear interface. The data shown here are for $H = 1$ and $R_T = 3.4$ kg/(s mm^4) (color figure online)

resistance of the trapped drop depends on the degree of blockage offered by the drop at the constriction. Figure 5b (i–v) shows the three-dimensional rendering of an image volume of 80 μm thickness (note trapped drop height is 200 μm) for selected capillary numbers. Until Ca ≤ 0.001, we observe that the trapped drop just sits near the constriction and does not fully block the constriction allowing suf-ficient flow of continuous phase through the microcavity and constriction. As a result, the hydrodynamic resistance offered by the trapped drop is low. Images shown in Fig. 5b-i, ii also show that the thickness of the continuous phase fluid layer near the rear end of the drop (i.e. toward constriction) does not vary appreciably for Ca ≤ 0.001, indicating

that the resistance is almost constant, consistent with *state I* shown in Fig. 5a.

When Q_M is further increased (Ca > 0.001), the drop starts to deform against the wall of the microcavity and penetrates into the constriction (see images in Fig. 5b-iii, iv). This penetration causes the continuous phase fluid layer to thin at the entrance of the constriction and increase the blockage significantly. As a result, the resistance of the trapped drop starts to increase significantly for Ca > 0.001, giving rise to the transition zone. At Ca ≥ 0.003, the trapped drop cannot deform anymore (than what it already has), and the maximum penetration of the finger (Fig. 5b-v) causes saturation in the drop resistance, giving rise to *state II*.

Additionally, we find that the continuous phase fluid layer at the entrance of the constriction has almost vanished (within the resolving power of the microscope imaging) indicating that resistance saturates when the maximum penetration of the drop finger is achieved.

Similar to experiments using simulations, we examined the drop deformation and continuous fluid layer around the drop for $\alpha = 0.6$. The images in Fig. 6a–c show the trapped droplet and the continuous phase layer for different views in the channel, at different capillary numbers. Figure 6b shows the droplet's cross section at half height of the channel in the x–y plane. We observe that by increasing Ca, the droplet gets pushed toward the front wall of the trap and starts to penetrate into the constriction. At low Ca (Ca < 0.001), the constriction is free from blockage. On the other hand, at high Ca (Ca > 0.001), the droplet blocks the constriction. These results are consistent with the experimental observations from confocal imaging.

Unlike confocal imaging, we are able to extract additional views of drop deformation from the numerical simulation analysis. Figure 6c shows the cross-sectional view of the constriction at different capillary numbers in the y–z plane. For Ca < 0.001, we observe that the cross section is empty as the droplet has not penetrated into the constriction and only the continuous phase is flowing through yielding a low resistance of the trapped drop (Fig. 6d). By increasing Ca, the droplet begins to penetrate into the constriction and the amount of blockage increases. At the highest Ca ($= 1.8 \times 10^{-2}$), the constriction is mostly filled with the droplet and the continuous phase only flows through the gutter region, generating high droplet resistance.

In Fig. 6a, we illustrate the end-view of the continuous phase flow around the droplet in the trap (note that the droplet phase in blue is not shown in these images). At low Ca, the continuous fluid layer is uniform around the droplet. On the other hand, at high Ca, the droplet gets pushed to the front wall of the trap and continuous phase film appears to get ruptured. By increasing the Ca, the size of the film rupture increases. The appearance of film rupture might be due to the inability to resolve the mesh in the simulations down to the scale of sub-microns. Nevertheless, we can conclude that the continuous fluid layer has thinned down significantly at the entrance of the constriction compared to other regions, which results in higher hydrodynamic resistance at high capillary numbers.

Using simulations, we also evaluated the drop configuration for $\alpha = 1$. We observed that the fully confined drop is always blocking the constriction (data not shown). Even at small capillary numbers, the droplet blocks the constriction. Therefore, the hydrodynamic resistance is almost constant over the range of explored Ca. By increasing the Ca, the droplet penetrates more into the constriction, and at high Ca's we observe the film ruptures, similar to Fig. 6a. The

magnitude of the resistance of the trapped drop increases slightly with drop confinement (for $\alpha < 1$) and viscosity ratio in simulation (Fig. 6d). In addition, the viscosity and confinement of the droplet do not significantly influence the configuration of the gutters.

Supporting evidence for the protrusion of the drop interface into the constriction comes from monitoring the Laplace pressure jump (ΔP_L) at the rear and front (i.e. toward constriction) of the trapped drop. Figure 6e shows that the ΔP_L at the rear interface of the drop is almost constant as the radius of curvature changes negligibly. On the other hand, the Laplace pressure jump at the front interface shows a bistable behavior as the interface curvature is varying at the front, indicating that the changes in front interface curvature contribute significantly to the bistable behavior.

In summary, the basic picture that explains bistability observed in experiments and simulations is as follows: The bistability arises from two unique states of the droplet configuration in the trap. The system switches from low to high hydrodynamic resistance depending on whether the constriction is free of blockage or occupied by drop interface, respectively (Fig. 6d). At low capillary number, the resistance remains low and constant until the drop protrudes into the constriction corresponding to *state I*. While in *state II*, even though the gutter cross section keeps reducing with increase in capillary number, the resistance increases only slightly.

3.4 Behavior of the trapped drop in the transition zone

In experiments and simulations, we clearly observed a bistable behavior with respect to drop resistance. In between the two states, there is a transition zone. In experiments, we observe that in the transition zone the drop fluctuates between getting pushed into and out of the constriction. As a result, we find that experimentally determined flow rate in the constriction Q_T fluctuates in the transition zone as the inlet capillary number is varied (Fig. 7). This fluctuation in Q_T causes the pressure drop to vary in a complex manner in the transition zone (see Fig. 3a). The fluctuations in Q_T could be due to syringe pump-induced fluctuations which are known to occur at low injection flow rates (Korczyk et al. 2011; Li et al. 2014). In contrast to experiments, in simulations the transition zone is sudden and since there are no flow fluctuations, the system jumps from *state I* and *state II*.

4 Conclusions

In this study, we develop an experimental method using microfluidic parking loop coupled with particle tracking velocimetry to measure the pressure drop and flow resistance of a trapped drop without the use of microfluidic
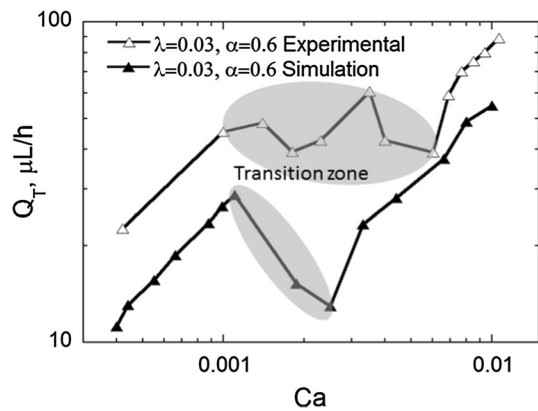
Fig. 7 The measured flow rate through the trapped channel (Q_T) is plotted as a function of the capillary number from experiments and simulations for viscosity ratio $\lambda = 0.03$ and drop confinement $\alpha = 0.6$. The transition zone is highlighted in gray

manometers (Abkarian et al. 2006; Vanapalli et al. 2007, 2009). In parallel, we implement VOF method to simulate the dynamics of a trapped drop in the microcavity.

Using these methods, we discover an interesting bistable behavior in terms of pressure drop and flow resistance of trapped drops that are smaller than the size of the microcavity. Depending on drop deformation at low and high Ca, the system can attain two states. At low Ca, the drop sits near the constriction without fully blocking it and allowing unobstructed flow of continuous phase fluid through it, whereas with increasing Ca, the drop starts penetrating into the constriction. At high Ca, the drop fully occupies the constriction and the continuous phase only flows through the gutter region. Thus, the system switches from low (*state I*) to high (*state II*) hydrodynamic resistance depending on whether the constriction is free or occupied, respectively. On the other hand, for a fully confined drop, the bistable behavior disappears, and we observe the *state II* pressure drop and flow resistance behavior only.

The underfilled drops in the microcavity act as nonlinear resistors since their resistance can be enhanced by a factor of 16 by switching the capillary number from low to high. This insight can be exploited in droplet-based microfluidic applications to control the trajectories of droplets. In a broader context, results from this study are also relevant for oil recovery applications where droplets are trapped in porous media (Gerritsen and Durlofsky 2005; Olbricht 1996) and for understanding the occlusion behavior of biological cells in microvascular networks (Higgins et al. 2007; Kienast et al. 2010).

References

Abkarian M, Faivre M, Stone HA (2006) High-speed microfluidic differential manometer for cellular-scale hydrodynamics. Proc Natl Acad Sci USA 103:538–542. doi:10.1073/pnas.0507171102

Bithi SS, Vanapalli SA (2010) Behavior of a train of droplets in a fluidic network with hydrodynamic traps. Biomicrofluidics 4:044110. doi:10.1063/1.3523053

Bithi SS, Vanapalli SA (2015) Collective dynamics of non-coalescing and coalescing droplets in microfluidic parking networks. Soft Matter 11:5122–5132. doi:10.1039/c5sm01077b

Bithi SS, Vanapalli SA (2017) Microfluidic cell isolation technology for drug testing of single tumor cells and their clusters. Sci Rep 7:41707. doi:10.1038/srep41707

Bithi SS, Wang WS, Sun M, Blawzdziewicz J, Vanapalli SA (2014) Coalescing drops in microfluidic parking networks: A multifunctional platform for drop-based microfluidics. Biomicrofluidics 8:034118. doi:10.1063/1.4885079

Boukellal H, Selimovic S, Jia YW, Cristobal G, Fraden S (2009) Simple, robust storage of drops and fluids in a microfluidic device. Lab Chip 9:331–338. doi:10.1039/b808579j

Bruus H (2008) Theoretical microfludics. Oxford University Press, Oxford

Dangla R, Lee S, Baroud CN (2011) Trapping microfluidic drops in wells of surface energy. Phys Rev Lett 107:124501. doi:10.1103/PhysRevLett.107.124501

Du W, Li L, Nichols KP, Ismagilov RF (2009) SlipChip. Lab Chip 9:2286–2292. doi:10.1039/B908978K

Duffy DC, McDonald JC, Schueller OJ, Whitesides GM (1998) Rapid prototyping of microfluidic systems in poly(dimethylsiloxane). Anal Chem 70:4974–4984. doi:10.1021/ac980656z

Edd JF, Humphry KJ, Irimia D, Weitz DA, Toner M (2009) Nucleation and solidification in static arrays of monodisperse drops. Lab Chip 9:1859–1865. doi:10.1039/B821785H

Fradet E, McDougall C, Abbyad P, Dangla R, McGloin D, Baroud CN (2011) Combining rails and anchors with laser forcing for selective manipulation within 2D droplet arrays. Lab Chip 11:4228–4234. doi:10.1039/C1LC20541B

Gerritsen MG, Durlofsky LJ (2005) Modeling fluid flow in oil reservoirs. Annu Rev Fluid Mech 37:211–238. doi:10.1146/annurev.fluid.37.061903.175748

Higgins JM, Eddington DT, Bhatia SN, Mahadevan L (2007) Sickle cell vasoocclusion and rescue in a microfluidic device. Proc Natl Acad Sci 104:20496–20500. doi:10.1073/pnas.0707122105

Hoang D, Portela L, Kleijn C, Kreutzer M, Van Steijn V (2013a) Dynamics of droplet breakup in a T-junction. J Fluid Mech 717:R4

Hoang DA, van Steijn V, Portela LM, Kreutzer MT, Kleijn CR (2013b) Benchmark numerical simulations of segmented two-phase flows in microchannels using the Volume of Fluid method. Comput Fluids 86:28–36

Huerre A, Theodoly O, Leshansky AM, Valignat M-P, Cantat I, Jullien M-C (2015) Droplets in microchannels: dynamical properties of the lubrication film. Phys Rev Lett 115:064501

Jeong H-H, Jin SH, Lee BJ, Kim T, Lee C-S (2015) Microfluidic static droplet array for analyzing microbial communication on a population gradient. Lab Chip 15:889–899. doi:10.1039/C4LC01097C

Kienast Y, von Baumgarten L, Fuhrmann M, Klinkert WEF, Goldbrunner R, Herms J, Winkler F (2010) Real-time imaging reveals the single steps of brain metastasis formation. Nat Med 16:116–122 doi:http://www.nature.com/nm/journal/v16/n1/suppinfo/nm.2072_S1.html

Korczyk PM, Cybulski O, Makulska S, Garstecki P (2011) Effects of unsteadiness of the rates of flow on the dynamics of formation

of droplets in microfluidic systems. Lab Chip 11:173–175. doi:10.1039/C0LC00088D

Korczyk PM, Derzsi L, Jakiela S, Garstecki P (2013) Microfluidic traps for hard-wired operations on droplets. Lab Chip 13:4096–4102. doi:10.1039/C3LC50347J

Lau BTC, Baitz CA, Dong XP, Hansen CL (2007) A Complete Microfluidic Screening Platform for Rational Protein Crystallization. J Am Chem Soc 129:454–455. doi:10.1021/ja065855b

Li Z, Mak SY, Sauret A, Shum HC (2014) Syringe-pump-induced fluctuation in all-aqueous microfluidic system implications for flow rate accuracy. Lab Chip 14:744–749. doi:10.1039/C3LC51176F

Ling Y, Fullana J-M, Popinet S, Josserand C (2016) Droplet migration in a Hele–Shaw cell: effect of the lubrication film on the droplet dynamics. Phys Fluids 28:062001. doi:10.1063/1.4952398

Nekouei M, Vanapalli SA (2017) Volume-of-fluid simulations in microfluidic T-junction devices: influence of viscosity ratio on droplet size. Phys Fluids 29:032007

Nieves-Remacha MJ, Yang L, Jensen KF (2015) OpenFOAM computational fluid dynamic simulations of two-phase flow and mass transfer in an advanced-flow reactor. Ind Eng Chem Res 54:6649–6659

Olbricht WL (1996) Pore-scale prototypes of multiphase flow in porous media. Annu Rev Fluid Mech 28:187–213. doi:10.1146/annurev.fl.28.010196.001155

OpenCFD O (2009) The Open Source CFD Toolbox User Guide. OpenCFD Ltd

Pompano RR, Liu WS, Du WB, Ismagilov RF (2011) Microfluidics using spatially defined arrays of droplets in one, two, and three dimensions. Annu Rev Anal Chem 4:59–81

Seemann R, Brinkmann M, Pfohl T, Herminghaus S (2011) Droplet based microfluidics. Rep Prog Phys 75:016601

Shemesh J et al (2014) Stationary nanoliter droplet array with a substrate of choice for single adherent/nonadherent cell incubation and analysis. Proc Natl Acad Sci 111:11293–11298. doi:10.1073/pnas.1404472111

Shi WW, Qin JH, Ye NN, Lin BC (2008) Droplet-based microfluidic system for individual Caenorhabditis elegans assay. Lab Chip 8:1432–1435. doi:10.1039/b808753a

Sun M, Bithi SS, Vanapalli SA (2011) Microfluidic static droplet arrays with tuneable gradients in material composition. Lab Chip 11:3949–3952. doi:10.1039/C1LC20709A

Vanapalli SA, Dvd Ende, Duits MHG, Mugele F (2007) Scaling of interface displacement in a microfluidic comparator. Appl Phys Lett 90:114109. doi:10.1063/1.2713800

Vanapalli SA, Banpurkar AG, van den Ende D, Duits MHG, Mugele F (2009) Hydrodynamic resistance of single confined moving drops in rectangular microchannels. Lab Chip 9:982–990. doi:10.1039/B815002H

Zagnoni M, Cooper JM (2010) A microdroplet-based shift register. Lab Chip 10:3069–3073. doi:10.1039/C0LC00219D

Zhang C, Xing D (2010) Single-molecule DNA amplification and analysis using microfluidics. Chem Rev 110:4910–4947

Zhu L, Gallaire F (2016) A pancake droplet translating in a Hele–Shaw cell: lubrication film and flow field. J Fluid Mech 798:955–969. doi:10.1017/jfm.2016.357